Accepted Manuscript

Title: Fractal Scan Strategies for Selective Laser Melting of 'Unweldable' Nickel Superalloys

Authors: S. Catchpole-Smith, N. Aboulkhair, L. Parry, C. Tuck, I.A. Ashcroft, A. Clare

This is a PDF file of an unedited manuscript that has been accepted for publication. As a service to our customers we are providing this early version of the manuscript. The manuscript will undergo copyediting, typesetting, and review of the resulting proof before it is published in its final form. Please note that during the production process errors may be discovered which could affect the content, and all legal disclaimers that apply to the journal pertain.

Fractal Scan Strategies for Selective Laser Melting of 'Unweldable' Nickel Superalloys

S. Catchpole-Smith[a], N. Aboulkhair[a], L. Parry[a], C. Tuck[a], I.A. Ashcroft[a], A. Clare[a,b]

[a]Additive Manufacturing & 3D Printing Research Group, The University of Nottingham, Nottingham, NG7 2RD, U.K.

[b]Advanced Manufacturing Group, Faculty of Engineering, The University of Nottingham, Nottingham, NG7 2RD, U.K.

ABSTRACT

The high thermal gradients experienced during manufacture via selective laser melting commonly result in cracking of high γ/γ' Nickel based superalloys. Such defects cannot be tolerated in applications where component integrity is of paramount importance. To overcome this, many industrial practitioners make use of hot isostatic pressing to 'heal' these defects. The possibility of such defects re-opening during the component life necessitates optimisation of SLM processing parameters in order to produce the highest bulk density and integrity in the as-built state.

In this paper, novel fractal scanning strategies based upon mathematical fill curves, namely the Hilbert and Peano-Gosper curve, are explored in which the use of short vector length scans, in the order of 100 µm, is used as a method of reducing residual stresses. The effect on cracking observed in CM247LC superalloy samples was analysed using image processing, comparing the novel fractal scan strategies to more conventional 'island' scans. Scanning electron microscopy and energy dispersive X-ray spectroscopy was utilised to determine the cracking mechanisms. Results show that cracking occurs via two mechanisms, solidification and liquation, with a strong dependence on the laser scan vectors. Through the use of fractal scan strategies, bulk density can be increased by 2±0.7 % when compared to the 'island' scanning, demonstrating the potential of fractal scan strategies in the manufacture of typically 'unweldable' nickel superalloys.

Keywords: selective laser melting, Nickel alloys, scan strategies, Additive Manufacture.

1   INTRODUCTION

1.1   Selective Laser Melting

Selective laser melting (SLM) utilises a computer-controlled scanning laser beam to manufacture complex components by melting metallic powder in a layer-by-layer fashion, direct from a 3D computer

model. A wide range of Ti [1, 2], Fe [3, 4], Ni [5, 6], and Al [7, 8] alloys have been processed via SLM, with near 100% bulk density and good mechanical performance. Ni alloys are of significant interest to SLM users for their performance in the high-temperature, load-bearing environments found in the aero and industrial gas turbine industry. They are the materials of choice for hot gas path components due to their excellent creep and thermal fatigue strength, oxidation resistance and hot corrosion resistance [9]. Some examples of such components are turbine blades, discs, vane segments and casings. CM247LC [10] was initially developed as a directional solidification nickel alloy for the investment casting of turbine blades, particularly designed for high creep strength. It is a low carbon derivative of MAR-M-247 with reduced Zr and Ti content, and tightened control on Si and S. CM247LC consists of a γ/γ' dual-phase, face-centred cubic (FCC) crystal structure with preferential solidification in the <001> direction. Its strength arises from the precipitation of the coherent intermetallic γ'-phase, with basic composition $Ni_3(Al, Ti)$, within the γ nickel matrix. Addition of refractory elements facilitates the precipitation of primary metallocarbohedryne (MC) type carbide structures (preferentially TaC, TiC and HfC) [11] to the grain boundaries; these phases, through pinning mechanisms, prevent slip and hence improve creep resistance.

Nickel alloys with high γ/γ' volume fraction often exhibit poor weldability, a term used to denote high propensity for cracking, due to their sensitivity to high thermal gradients. The 'weldability' of Ni alloys can be considered as a function of the content of γ'-phase forming elements, Al and Ti, as shown in Figure 1, where an alloy with Al + Ti composition >4.5 Wt% can typically be considered 'unweldable' [12]. SLM combines a high energy density laser source with high traverse speeds, with the resultant high thermal gradients producing thermally induced residual stresses. Hence, conventional SLM scan strategies are particularly unsuitable for the processing of such 'unweldable' alloys.

The poor weldability of CM247LC results in the need for post-processing to heal defects present in SLM manufactured samples. Hot isostatic pressing (HIPing), as discussed by Kunze et al. [13] for IN738LC and by Carter et al. [14] for CM247LC, has been shown to close micro-cracks. However, post-HIP processing, precipitate traces have been observed in the regions of healed crack zones in samples produced via Laser Solid Forming (LSF), with precipitate coarseness proportional to the original length of the crack [15]. Zhao et al. [15] concluded that the diffusion bonding mechanism on

which HIPing acts is not sufficient to eliminate segregation of carbide forming elements, hence these weakly bonded regions remain post-HIP. Thus, it is desirable to minimise the cracking density in the as-deposited part in advance of any subsequent processing; the success of crack healing via HIPing is directly related to the integrity of the material at the condition of supply.

A conventional method of reducing build-up of residual stresses is to divide the laser scanned area of each layer into smaller square sections referred to as 'islands', comprised of a border (contour) and inner raster scan region. Lu et al. [16] conducted a comprehensive analysis on the effect of varying the 'island' sizes when processing IN718. It was seen that reducing the 'island' size below 3 x 3 mm produced a significant increase in cracking density, as the large number of 'island' intersections resulted in poor metallurgical bonding. Variation in cracking density using 'island' scanning in CM247LC deposits was reported by Carter et al. [17]. This was attributed to a bimodal grain structure, consisting of columnar grains aligned with the build direction surrounded by fine equiaxed grains positioned along the intersection of the scanned 'islands'. The high cracking density within the fine equiaxed region precluded 'island' scanning from being an effective method in this case.

Despite these issue with 'island' scanning, there has been only limited exploration of alternate scanning strategies, such as mathematical area filling curves, or 'fractals'. Ma et al. [18] simulated the temperature and stress variations seen during selective laser sintering (SLS) of polymer powder, comparing a standard meander scanning pattern to the Hilbert 'fractal' scanning pattern. It was concluded that the Hilbert scan pattern produces a more symmetrical temperature field and smaller plate distortion than the meander scan pattern. Further SLS simulation tests by Yang et al. [19] also concluded that the use of the Hilbert curve results in lower thermal gradients and decreased residual stress in SLS components. Experimental tests indicated more consistent sintering and higher tensile strength in components manufactured using Hilbert curve scanning strategies. Currently, no literature details the application of fractal scan strategies to metal additive manufacturing (AM) processes, specifically SLM. In this paper, novel scanning strategies based on fractals are developed as a method of reducing the residual stress build-up responsible for cracking in CM247LC samples manufacture by selective laser melting. Currently, no data is available on how fractal scan strategies influence integrity post SLM, however the in-situ methods for reducing thermal gradients in SLS demonstrated by Ma et al. [18] and

Yang et al. [19] can be transferred to SLM. The typical SLM optimisation techniques involving laser power and scan speed parameters have proved to be of limited effect in reducing cracking for CM247LC. Hence, more sophisticated scan strategies are required that consider the development of the thermal gradients responsible for stress induced cracking. Such scan strategies may be necessary for the manufacture of high-density components in the as-SLM state, eliminating or minimising the need for post-processing steps such as HIPing.

2   MATERIALS AND METHODS

2.1   CM247LC

The powder used for experimentation was supplied by LPW Technology Ltd. Analysis with a Malvern Mastersizer 3000 indicated the particle size distribution seen in Figure 2 (a) with range 15-100µm, D_{10} = 20 µm, D_{50} = 36.4 µm, and D_{90} = 57.1 µm. Scanning electron microscopy (SEM) micrographs of the bulk powder confirmed a morphology characteristic of the gas atomisation powder manufacturing method. These properties are conducive to satisfactory flowability and close packing density in the powder bed. Despite the presence of many irregular shaped particles dispersed throughout Figure 2(b), the powder was determined to have a good flowability index of 14.62± 0.4 s/50g, using a Hall flowmeter funnel in accordance with the ASTM standard B213 [20]. The elemental composition of the virgin powder was analysed by energy dispersive X-ray spectroscopy (EDX) using an Oxford Instruments X-Max Silicon Drift Detector, with the composition given in Table 1, calculated as an average of three square maps with a count time of 300 second per map. It can be seen that the actual composition of the feedstock has a decreased weldability than the nominal composition due to the greater quantity of aluminium and titanium. Overall, the actual feedstock has a greater contribution of every alloying element except for tungsten when compared to the nominal composition. Some elements could not be quantified due to the low concentrations and detection limits of the EDX sensor.

2.2   *Selective Laser Melting*

All samples were manufactured using a Realizer SLM 50 equipped with an IPG Photonics continuous wave ytterbium fibre laser (YLM-100-AC) source with a wavelength of 1070 nm and a maximum power output of 100 W. During processing, the build chamber was purged and continuously flushed with argon to create a working environment of <0.5 vol% O_2 to inhibit oxidation. The build platform was maintained at 200 °C for the duration of the build to control heat conduction through the substrate. This is a commonly used method to help reduce distortion resulting from thermally induced stresses in SLM.

2.3   *Scan Strategies*

In this study, an 'island' scan sample was produced with dimensions 10 x 10 x 5 mm [*XYZ*], with the *XY* plane divided into four equal 5 x 5 mm discrete 'islands' (*see* Figure 3). This island size was determined to be optimal by Lu et al. [16] and was also consistent with the samples produced by Carter et al. [17], [21]. Initially, the entire 10 x 10 mm sample cross-section was contour scanned to give a single track thickness wall around the perimeter, then the 'island' regions were in-filled using a raster scan, as illustrated in Figure 3. Samples were produced using a 25 µm layer thickness, 100 W laser power and a 400 mm.s^{-1} scan speed, determined to be the optimum processing parameters in an earlier parametric study. This sample was used as the baseline for comparison with the novel fractal scan strategies as it is an established method of reducing residual stresses in SLM manufacture.

A range of samples were manufactured using novel fractal scanning strategies based upon the mathematical area filling curves *Hilbert* [22] and *Peano-Gosper* [23]. The characteristic scan vector length in each case was defined as 100 µm, whilst no single vector length was permitted to exceed 300 µm; illustrations of the fractal scan strategy paths are shown in Figure 4. The relationship between scan vector length and residual stress was explored by Kruth et al. [24]. An indicator of residual stress, curling angle, was correlated with scan vector length, where it was seen that using 2 mm vector lengths provided a 13% reduction in curling angle compared to a reference part manufactured using 20 mm vector lengths. However, no experiments were conducted using shorter vector lengths. Parry et al. [25]

identified that longitudinal residual stress increases with scan vector length, hence reducing the vector length as far as possible should prevent the stress build-up that results in cracking for 'unweldable' Ni superalloys such as CM247LC. The use of short vector lengths to reduce residual stress underlies the 'island' scanning strategy, however, this can result in anisotropic stress distribution over a part cross-section due to differentials in temperature distribution at the ends of the scan vectors. Hence, simply substituting short vector lengths into 'island' patterns may not result in an overall stress reduction. However, application of a fractal scan pattern, as a single, continuous path that covers a wide area, can potentially provide a more uniform temperature distribution compared to the cyclic heat input that is associated with unidirectional, straight line raster fill scans.

A MATLAB script was used to add appropriate laser spot size and hatch spacing parameters to the fractal curve generation code for use in an SLM application. The script also defined material and process parameters and output a machine file directly readable by the SLM machine. With the hatch spacing defined as 50 µm, the resultant samples were formed by a single continuous scan path that filled an area of 5 x 5 mm and 3.3 x 3.3 mm for the Hilbert and Peano-Gosper paths, respectively. For each fractal scan strategy, scan speeds of 500, 600, 700 and 800 mm.s^{-1} and laser powers of 75 W and 100 W laser were used to explore the processing envelope. A summary of the process parameter sets is given in Table 2. The samples were produced with 25 µm layer height and a total height of 5 mm excluding strut support structures.

2.4   Sample Preparation

After manufacture, the samples were cross-sectioned in the *XY* and *YZ* planes. The cross-sections were ground and polished following typical metallographic preparation techniques. The samples were then etched using Kalling's No. 2 reagent (5 g $CuCl_2$, 100 ml HCl, 100 ml ethanol). This revealed any crack or pores in the sample, the structure of the track deposits characteristic of the SLM process and the resulting microstructure that formed as the material solidified.

2.5   Crack and Pore Density Analysis

A high resolution, wide-area view of each polished cross-section was captured using a Nikon Eclipse LV100ND optical microscope. To analyse the cracking and porosity within the samples, the image processing software core package ImageJ [26] with the Fiji plugin bundle [27] was used, following the image processing steps outlined in Figure 5. A threshold was applied to each region of interest (ROI) to isolate the cracks and pores, followed by a noise reduction step. The cracks and pores were then isolated independently by applying geometrical constraints and the data was exported for quantification of defects and sample density.

Further examination of the microstructure was performed using a Philips XL30 SEM in order to assess the morphology of grains and capture high resolution micrographs of surfaces of interest. An Oxford Instruments X-Max Silicon Drift energy-dispersive X-ray spectroscopy (EDX) detector was used to perform line scans across cracks in an attempt to capture any elemental variation at the crack boundaries.

3   RESULTS AND DISCUSSION

3.1   Crack locations and morphology

All sample builds were superficially successful, with no warping or lifting from the support structures and no macro-scale surface cracking or porosity. However, micro-cracking was prevalent in every case. In the 'island' scan control sample, cracking and porosity varied greatly within the cross-section, particularly at the 'island' intersection region, where defects were most prevalent. These bands of low density were associated with long cracks predominantly parallel to the border of each island, along with smaller cracks perpendicular to the border that extended into the bulk area (Figure 6). In the 'island' raster fill area, the cracking has a distinct directionality that followed the laser scan vector; i.e. a cracking pattern at 0° and 90° to the sample edges as a result of the 90° rotation of the raster fill scan between each layer.

In the fractal scan samples, the origin and appearance of large cracks occurred in approximately the same place for every sample in the *XY* plane (see Figure 7), across all process parameter sets. Further,

the cracking did not follow the scan vector lines as in conventional scanning strategies, as evident when overlaying the scanning strategy onto the deposit micrograph, as in Figure 8. This indicates that very repeatable stress concentration points are developed by the fractal scan patterns. In the Hilbert samples, cracking occurred along scan vectors but also at an angle to the scan vectors, indicating that the build-up of residual stress in the fractal samples is more complex as a result of the rapidly varying scan vectors. Cracking is also multi-directional in the Peano-Gosper samples, however this is to be expected due to the addition of a scan vector that is at a 65° angle to the *X* or *Y* axis. It is hypothesised that the cracking seen here is as a result of localised micro-scale stress vectors combining to form stress concentration points. As a result, cracks can form at an angle to or perpendicular to the direction expected from conventional understanding of stress build-up using long vector length scans. The stress concentration theory would explain the propensity for crack initiation and growth in the same location and direction for each fractal scan sample. In the *YZ* plane, large cracks were seen parallel to the build direction and frequently coalesced to form one continuous crack, spanning the full height of the deposit in a number of cases. Some deposits contained a number of these long cracks whilst others contained single, typically longer and wider, cracks.

3.2 *Microstructure and cracking mechanisms*

The Ni-based superalloy CM247LC is susceptible to two main types of cracking during SLM processing: solidification cracking and grain boundary liquation cracking. Solidification cracking can occur in the fusion zone of a melt pool where the newly deposited material is cooling at a higher rate than the surrounding material. Alloys with a large number of alloying elements tend to have a wide solidification temperature range and hence are more susceptible to solidification cracking. As the melt pool cools, partial solidification of the lower melting point elements forms a two-phase liquid-solid composition [28], resulting in a low energy path for crack propagation. Liquation cracking can occur during SLM in the partially-melted zone created when solid material in a previous layer is re-melted by the laser beam when processing the current layer [29], again providing a low energy path for cracking.

However, in this case cracking occurs in the previously solidified material. Due to both mechanisms acting along the grain boundaries, the microstructure is particularly significant when analysing cracking in CM247LC, as discussed in the next paragraph.

In the *XY* plane, a bi-modal grain structure was formed consisting of a mix of fine and coarse equiaxed grains for the 'island' and fractal scan samples. Cracking occurred where coarse equiaxed grains intersected fine grain regions (Figure 9, (a)), or where a colony of large equiaxed grains ruptured to form a crack (Figure 9, (b)). The bi-modal structure appeared to have no obvious pattern in the *XY* plane. In the fractal scan samples, the complexity of the rapidly changing ~100 μm scan vectors formed a cooling regime that had no preferential grain growth direction in the *XY* plane. This may serve to remove any obvious patterning. In the 'island' samples, a 90° rotation of the raster fill scan between each layer resulted in a cross-over of the laser scan vectors, preventing growth of the distinct grain texture that results from using equal scan vectors in each layer. However, despite Divya et al. [30] using a 67° rotation of the scans between layers, a bi-modal grain structure was clearly visible in their samples in the *XY* plane using the EBSD analysis, suggesting that a higher laser energy density can result in preferential grain growth regardless of rotation between layers.

Some precipitates were observed at grain boundaries and appear as bright spots in the backscatter electron images due to their high atomic mass (Figure 9, (c)). The precipitates can be found uniformly distributed within the bulk material and despite their common occurrence along crack boundaries, there was no clear indication that they were the sole cause of crack initiation or higher crack formation propensity. To investigate the possibility of carbide thin films at crack boundaries, EDX line scans were taken across crack boundaries and assessed for elemental concentrations, as seen in Figure 10. Cloots et al. [31] suggested that Zr may be responsible for solidification cracking in SLM processed IN738LC as it acts to significantly lower the solidus temperature at grain boundaries. However, EDX line scans showed no peaks in Zr elemental concentration near the crack boundaries in this work. Further, no peaks

corresponding to carbide forming elements were seen at the crack boundaries, indicating that no thin-film of carbides is initiating cracking. Drop-off and pick-up signals of elements such as Ti, Mo and Zr can be seen at the crack boundaries, however such trends follow that of major constituents such as Al and Ti and hence do not indicate elemental concentration greater than that seen in the bulk material.

In the *YZ* plane, cracking appears to follow grain boundaries with preference for regions where longer, columnar grains interact with shorter, more equiaxed grains (Figure 11, (a)). This bi-modal grain structure was repeatedly identifiable in the *YZ* direction as coarse columnar grains at the core of each melt pool and fine equiaxed grains at the boundary. This follows on from the theoretical understanding of melt pool cooling, in which the core material retains heat and hence cools at a slower rate than the boundary. The fast cooling boundary solidifies as fine grains whilst the core has sufficient time to form a columnar grain structure. Further, the directional growth of columnar grains from the core of the melt pool follows the expected path parallel to the greatest heat flux lines, extending towards the heat source.

For shorter, more isolated cracks, particularly those only spanning the height of a single build layer, the mechanism of solidification cracking is supported by the appearance of cracks clearly separating individual columnar dendritic grains in the *YZ* direction as seen in Figure 11 (b). These solidification cracks can act as initiation sites for liquation cracking as the build continues. The serrated, deformation-free appearance and mirrored morphology of the crack surfaces either side of the cracks shown in Figure 11 (c) suggests cracking after partial re-melting, characteristic of liquation cracking [32]. In consecutive layers, these liquation cracks are repeatedly partially re-melted, initiating further crack growth that extends through multiple build layers, as evident in Figure 11 (a). It is difficult to attribute a single cracking mechanism to each crack, particularly as solidification and liquation cracking act via similar mechanisms and both follow grain boundaries, however, there is evidence of both cracking mechanisms acting in the samples, particularly in the *YZ* plane.

3.3   *Quantitative density analysis*

The crack length density (total length of cracks per bulk area) and crack area density (total area of cracks per bulk area) were calculated separately. The distinction between crack length density and crack area density was made as using crack length alone does not necessarily reflect the severity of cracking within a sample. For example, narrow cracks will respond more favourably to HIPing than wide cracks. Separating the measurements provides a better representation of the condition of the as-built SLM samples, as well as a secondary metric to compare the scanning strategies used in the experiments. The bulk density of each sample was calculated by subtracting the crack and pore area from the bulk sample area analysed.

The overall bulk density data for all samples is given in Figure 12. The highest XY plane bulk density of 98.0±0.1 % was achieved using the Peano-Gosper scan at 75 W laser power and 600 mm.s^{-1} scan speed. This is significantly higher than the XY plane bulk density of the 'island' scan sample at 96.0±0.6 %. This is attributed to the large amount of spherical porosity seen in the 'island' sample, whereas porosity was rarely seen in any of the fractal scan samples. Further, the fractal scan samples typically had less variation in the bulk density across the three ROI analysed when compared to the 'island' scan sample. In the YZ plane, the bulk density of the fractal samples was also significantly higher than the 'island' sample. However, the variation in density is larger due to difficulty in repeatable cross-sectioning of the samples; the complex scan strategy results in a higher propensity for YZ plane cracking in some regions and so crack density can vary depending on the location of the cross-section taken.

When comparing the crack length density in Figure 13, it is again clear that the fractal scan samples provide an improvement over the 'island' scan. Overall, the crack length density was lower in the YZ plane than the XY plane, as expected from the bulk density results. For every process parameter set, the upper and lower bounds of the crack length density measurements overlap, indicating that the two fractal scan strategies are very similar in cracking propensity due to their thermal profile and hence stress build up within the sample. The lowest mean XY plane crack length density of 0.82±0.40 mm/mm^2 was in the Hilbert scan, 100 W and 700 mm.s^{-1}, compared to 2.71±0.47 mm/mm^2 for the 'island' sample.

The crack length density was also the lowest using this Hilbert fractal scan, providing an even greater magnitude of improvement over the 'island' sample. Again, the samples show a greater variation in *YZ* plane crack length density across the process parameter sets, attributed mainly to the differences in cross-sectioning. However, the results still demonstrate the improvement made by the fractal scans to reduce the prevalence of cracks in the CM247LC samples.

Finally, the crack area density for each sample is given in Figure 14. The importance of differentiating between crack length and crack area is evident by the less significant improvement made by the fractal scan samples. However, a reduction in crack area density was still seen in 81 % of the *XY* plane and 94 % of the *YZ* plane of the fractal scan samples, demonstrating that the novel scan strategies are effective across all quantification metrics used in this study. The crack area density data confirms the observation from the optical micrographs that the cracks in the fractal samples are shorter, but wider than those seen in the 'island' samples. This could pose a problem for HIP treatment whereby wide cracks cannot be fully consolidated. However, the cracks are still in the micro-scale with a typical width <50 μm. Of greater value from the fractal scan samples is the reduction in the crack length density and hence the reduction in the number of healed sites that would remain post-HIP. Such heal sites often contain thin films of precipitates, such as carbides, which result in a weakly bonded interface [15] that is susceptible to re-opening during the service life of the component. Hence, the reduction in crack length density that the fractal scan strategies can provide is more desirable than a reduction in crack area density. Further, the fractal scans also resulted in a large reduction in porosity and hence the bulk density was significantly greater than in the 'island' samples, highlighting the benefit of using fractal scans for porosity reduction as well as crack reduction. As such, fractal scans may also be beneficial when applied to alloys where the principal density issue is porosity rather than cracking.

3.4   *Fractal scans for end-use manufacture*

Of significance from this study is the dependence of the crack morphology, position and direction on the scan strategy, or more specifically, the scan vector. The novel fractal scan strategies demonstrated here, whilst still resulting in cracked samples, produce a repeatable defect pattern. With knowledge of

how cracks may develop in each scenario, defects could be more reliably detected and potentially resolved in-situ during the build, effectively reducing the number of scrap parts manufactured. Further, there exists the possibility to apply different scanning strategies to individual areas of a part cross-section dependent upon crack susceptibility, as a result of part geometry, to reduce the probability of cracks developing in these areas. Eliminating cracking is of paramount importance for the manufacture of components via SLM. Whilst HIPing can improve the density post-SLM, defects will remain that are susceptible to re-opening during service. This is especially significant for load-bearing components that undergo thermal cycling, where potential catastrophic failure could result. Conventional scan strategies have limited scope for optimisation, relying on laser power and scan speed as the primary parameters. Hence, novel scan strategies, such as the fractal scans proposed here, should be explored further.

4   CONCLUSIONS

Novel fractal scan strategies based upon the Hilbert and Peano-Gosper curves have been developed and experimentally tested via SLM. Comparison with conventional 'island' scan samples shows that a significant increase in bulk density can be achieved by implementing the fractal scans. Optical micrographs and quantification of cracking data was used to highlight the importance of using multiple metrics to assess cracking to determine material quality. The following conclusions were drawn from the study:

- Cracking follows scan vectors in 'island' scanning with long vector lengths, but with fractal scan strategies, cracks often propagate parallel to and at an angle to the scan vectors

- Process parameter optimisation for 'island' scan strategies must consider the intersection region in order to achieve isotropic material density

- Crack origins and paths are repeatable in the fractal scan samples, irrespective of process parameters

- Sub-micron scale precipitates exist throughout the microstructure but are not necessarily responsible for crack initiation. This is supported by a lack of elemental concentration in EDX line scans across crack boundaries

- Partial re-melting of previously consolidated layers drives liquation cracking, resulting in cracks that span multiple build layers

- Crack length density and crack area density should be analysed separately in order to accurately determine the quality of a sample; bulk density alone is not sufficient

- The presence of porosity is independent of cracking and can be eliminated by implementing fractal scan strategies

The basis for implementing fractal scan strategies within SLM has been explored here. Due to the increased complexity compared to 'island' scan strategies, further optimisation must be performed to exploit the greatest reduction in cracking density of CM247LC samples. New fractal patterns may be introduced depending upon component cross-sectional area or presence of geometrical features such as thin walls, increasing the efficacy of their implementation further. For the current generation of SLM machines, fractal scan strategies show promise as a method of controlling the thermal profile of the process without the requirement for external heating of the build volume.

5 ACKNOWLEDGMENTS

6   REFERENCES

[1] I. Maskery, A.O. Aremu, M. Simonelli, C. Tuck, R.D. Wildman, I.A. Ashcroft, R.J.M. Hague, Mechanical Properties of Ti-6Al-4V Selectively Laser Melted Parts with Body-Centred-Cubic Lattices of Varying cell size, Experimental Mechanics 55(7) (2015) 1261-1272.

[2] M. Simonelli, Y.Y. Tse, C. Tuck, On the Texture Formation of Selective Laser Melted Ti-6Al-4V, Metallurgical and Materials Transactions A 45(6) (2014) 2863-2872.

[3] M. Garibaldi, I. Ashcroft, M. Simonelli, R. Hague, Metallurgy of high-silicon steel parts produced using Selective Laser Melting, Acta Materialia 110 (2016) 207-216.

[4] B. Liu, Further process understanding and prediction on selective laser melting of stainless steel 316L, Loughborough University, 2013.

[5] K.A. Mumtaz, P. Erasenthiran, N. Hopkinson, High density selective laser melting of Waspaloy®, Journal of Materials Processing Technology 195(1–3) (2008) 77-87.

[6] T. Vilaro, C. Colin, J.D. Bartout, L. Nazé, M. Sennour, Microstructural and mechanical approaches of the selective laser melting process applied to a nickel-base superalloy, Materials Science and Engineering: A 534 (2012) 446-451.

[7] N.T. Aboulkhair, N.M. Everitt, I. Ashcroft, C. Tuck, Reducing porosity in AlSi10Mg parts processed by selective laser melting, Additive Manufacturing 1–4 (2014) 77-86.

[8] N.T. Aboulkhair, I. Maskery, C. Tuck, I. Ashcroft, N.M. Everitt, The microstructure and mechanical properties of selectively laser melted AlSi10Mg: The effect of a conventional T6-like heat treatment, Materials Science and Engineering: A 667 (2016) 139-146.

[9] R.C. Reed, C.M.F. Rae, 22 - Physical Metallurgy of the Nickel-Based Superalloys A2 - Hono, David E. LaughlinKazuhiro, Physical Metallurgy (Fifth Edition), Elsevier, Oxford, 2014, pp. 2215-2290.

[10] K. Harris, G. Erickson, R. Schwer, MAR M 247 Derivations—CM 247 LC DS Alloy, CMSX® Single Crystal Alloys, Properties and Performance, 5th Int. Symp, 1984, pp. 221-230.

[11] H.-E. Huang, C.-H. Koo, Characteristics and Mechanical Properties of Polycrystalline CM 247 LC Superalloy Casting, MATERIALS TRANSACTIONS 45(2) (2004) 562-568.

[12] M. Henderson, D. Arrell, R. Larsson, M. Heobel, G. Marchant, Nickel based superalloy welding practices for industrial gas turbine applications, Science and Technology of welding and joining 9(1) (2004) 13-21.

[13] K. Kunze, T. Etter, J. Grässlin, V. Shklover, Texture, anisotropy in microstructure and mechanical properties of IN738LC alloy processed by selective laser melting (SLM), Materials Science and Engineering: A 620 (2015) 213-222.

[14] L.N. Carter, M.M. Attallah, R.C. Reed, Laser Powder Bed Fabrication of Nickel-Base Superalloys: Influence of Parameters; Characterisation, Quantification and Mitigation of Cracking, Superalloys 2012 (2012) 577-586.

[15] X. Zhao, X. Lin, J. Chen, L. Xue, W. Huang, The effect of hot isostatic pressing on crack healing, microstructure, mechanical properties of Rene88DT superalloy prepared by laser solid forming, Materials Science and Engineering: A 504(1–2) (2009) 129-134.

[16] Y. Lu, S. Wu, Y. Gan, T. Huang, C. Yang, L. Junjie, J. Lin, Study on the microstructure, mechanical property and residual stress of SLM Inconel-718 alloy manufactured by differing island scanning strategy, Optics & Laser Technology 75 (2015) 197-206.

[17] L.N. Carter, C. Martin, P.J. Withers, M.M. Attallah, The influence of the laser scan strategy on grain structure and cracking behaviour in SLM powder-bed fabricated nickel superalloy, Journal of Alloys and Compounds 615 (2014) 338-347.

[18] L. Ma, H. Bin, Temperature and stress analysis and simulation in fractal scanning-based laser sintering, The International Journal of Advanced Manufacturing Technology 34(9) (2006) 898-903.

[19] J. Yang, H. Bin, X. Zhang, Z. Liu, Fractal scanning path generation and control system for selective laser sintering (SLS), International Journal of Machine Tools and Manufacture 43(3) (2003) 293-300.

[20] Standard Test Methods for Flow Rate of Metal Powders Using the Hall Flowmeter Funnel, ASTM International, 2013.

[21] L.N. Carter, K. Essa, M.M. Attallah, Optimisation of selective laser melting for a high temperature Ni-superalloy, Rapid Prototyping Journal 21(4) (2015) 423-432.

[22] D. Hilbert, Ueber die stetige Abbildung einer Line auf ein Flächenstück, Mathematische Annalen 38(3) (1891) 459-460.

[23] B. Mandelbrot, Fractals: form, chance and dimension, Fractals: form, chance and dimension., by Mandelbrot, BB. San Francisco (CA, USA): WH Freeman & Co., 16+ 365 p. 1 (1979).

[24] J.-P. Kruth, J. Deckers, E. Yasa, R. Wauthlé, Assessing and comparing influencing factors of residual stresses in selective laser melting using a novel analysis method, Proceedings of the Institution of Mechanical Engineers, Part B: Journal of Engineering Manufacture 226(6) (2012) 980-991.

[25] L. Parry, I.A. Ashcroft, R.D. Wildman, Understanding the effect of laser scan strategy on residual stress in selective laser melting through thermo-mechanical simulation, Additive Manufacturing 12, Part A (2016) 1-15.

[26] C.A. Schneider, W.S. Rasband, K.W. Eliceiri, NIH Image to ImageJ: 25 years of image analysis, Nat Meth 9(7) (2012) 671-675.

[27] J. Schindelin, I. Arganda-Carreras, E. Frise, V. Kaynig, M. Longair, T. Pietzsch, S. Preibisch, C. Rueden, S. Saalfeld, B. Schmid, J.-Y. Tinevez, D.J. White, V. Hartenstein, K. Eliceiri, P. Tomancak, A. Cardona, Fiji: an open-source platform for biological-image analysis, Nat Meth 9(7) (2012) 676-682.

[28] T.P. Mitchell, R. Sanderson, B.G. Dance, Electron beam welding of crack sensitive nickel super alloy MAR-M-002, Materials science forum, Trans Tech Publ, 2007, pp. 3985-3990.

[29] S. Kou, Solidification and liquation cracking issues in welding, Jom 55(6) (2003) 37-42.

[30] V.D. Divya, R. Muñoz-Moreno, O.M.D.M. Messé, J.S. Barnard, S. Baker, T. Illston, H.J. Stone, Microstructure of selective laser melted CM247LC nickel-based superalloy and its evolution through heat treatment, Materials Characterization 114 (2016) 62-74.

[31] M. Cloots, P.J. Uggowitzer, K. Wegener, Investigations on the microstructure and crack formation of IN738LC samples processed by selective laser melting using Gaussian and doughnut profiles, Materials & Design 89 (2016) 770-784.

[32] M. Zhong, H. Sun, W. Liu, X. Zhu, J. He, Boundary liquation and interface cracking characterization in laser deposition of Inconel 738 on directionally solidified Ni-based superalloy, Scripta Materialia 53(2) (2005) 159-164.

Figure 1 - 'Weldability' diagram for a range of Ni alloys as a function of their Ti and Al alloy element composition. Weldability is considered poor above the dashed line and deteriorates with increasing Ti and Al content. All data taken from associated alloy specification documents.
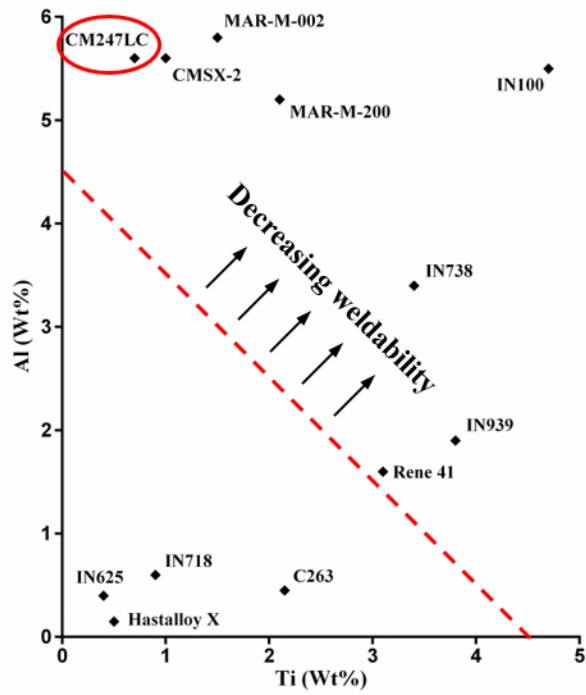
Figure 2 - a) CM247LC laser diffraction powder distribution histogram and b) SEM micrograph showing the largely spherical morphology but with many irregular shaped particles
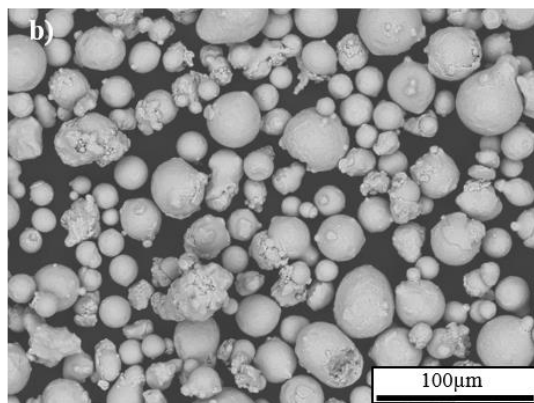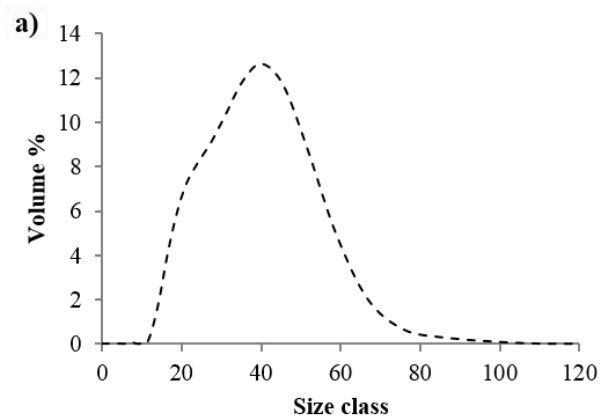
Figure 3 – Illustration of the 10 x 10 x 5 mm 'island' scan control sample. Initially, a single wall thickness contour scan is performed followed by the raster scans to form four 5 x 5 mm 'islands'
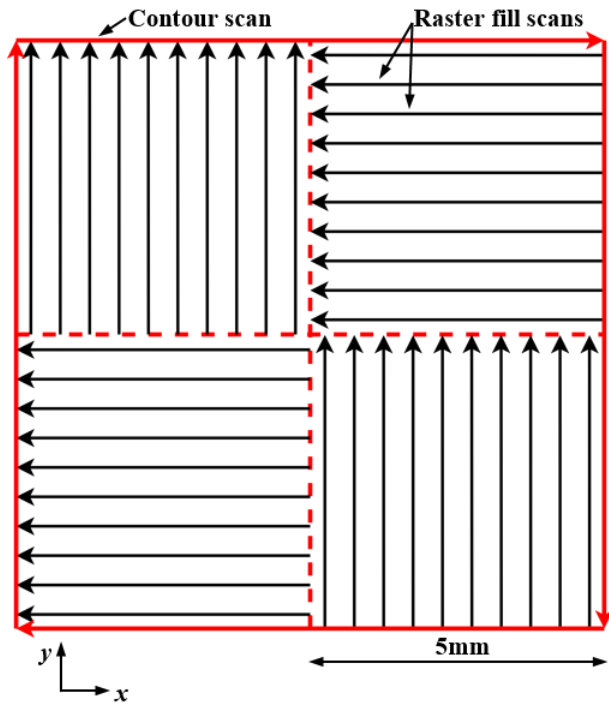
Figure 4 - Illustration of the novel scan strategies generated using the (a) 3rd order Hilbert and (b) 2nd order Peano-Gosper mathematical area filling curves. The 100μm characteristic scan vector length is shown
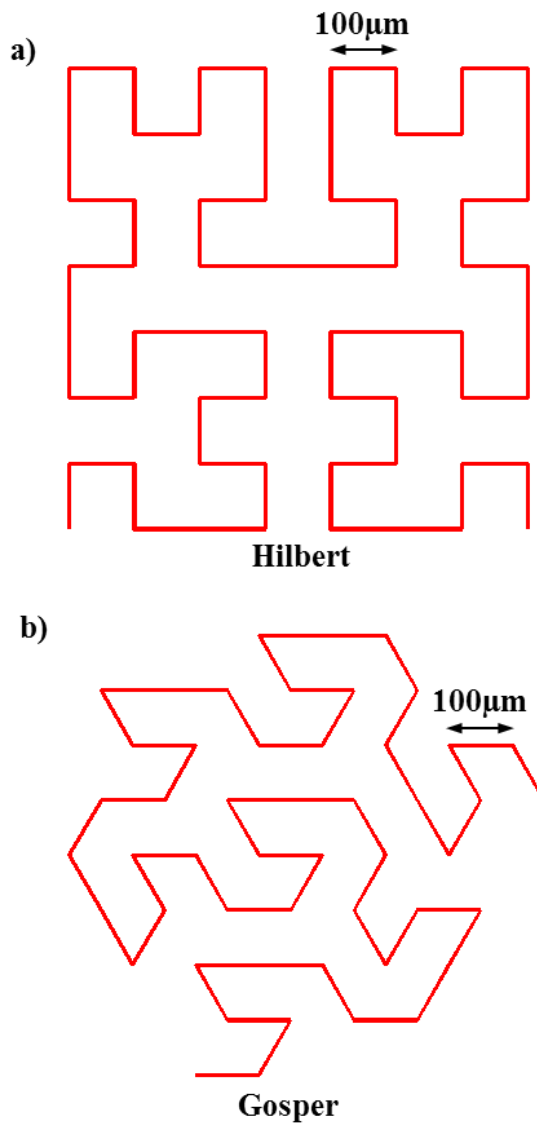
Figure 5 - Sequence for crack and pore filtering using image processing software ImageJ

Raw image   Threshold and despeckle

Filter pores   Filter cracks
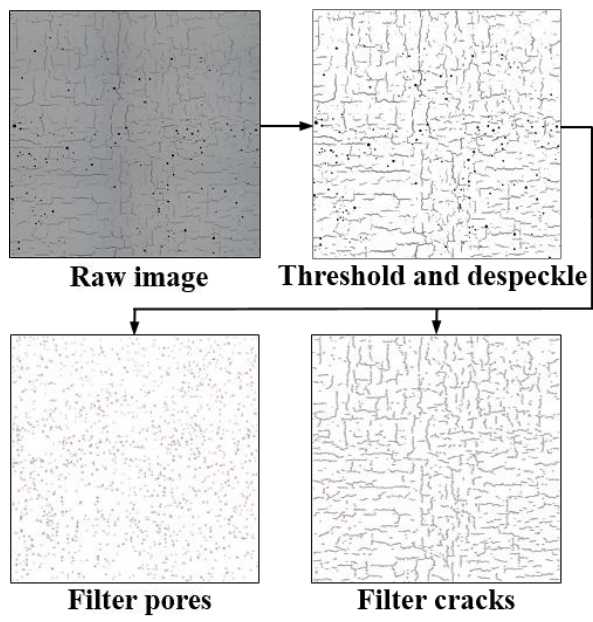
Figure 6 - Identification of the increased cracking and porosity regions in the 'island' intersections. Note that the cracking has a distinct directionality at 0° and 90° to the 'island' borders, aligned with the laser scan vectors
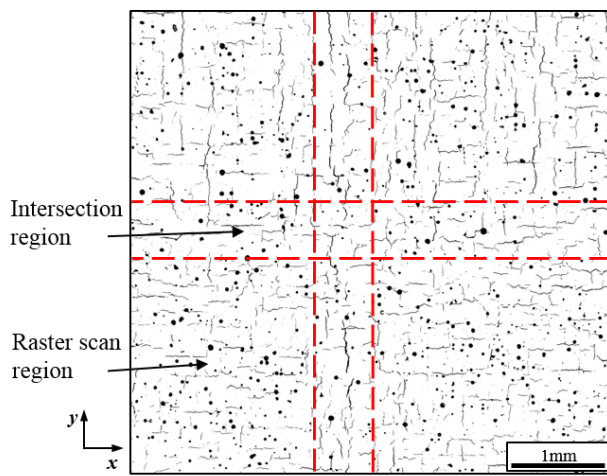
Figure 7 - Optical micrographs showing the highest density (left) and lowest density (right) of each fractal scan strategy type. (a) Hilbert 100 W, 600 mm.s^{-1}, (b) Hilbert 75 W, 500 mm.s^{-1}, (c) Peano-Gosper 75 W, 600 mm.s^{-1}, (d) Peano-Gosper 100 W, 500 mm.s^{-1}. CO = crack origin; note the very similar placement of cracking for each fractal scan type.
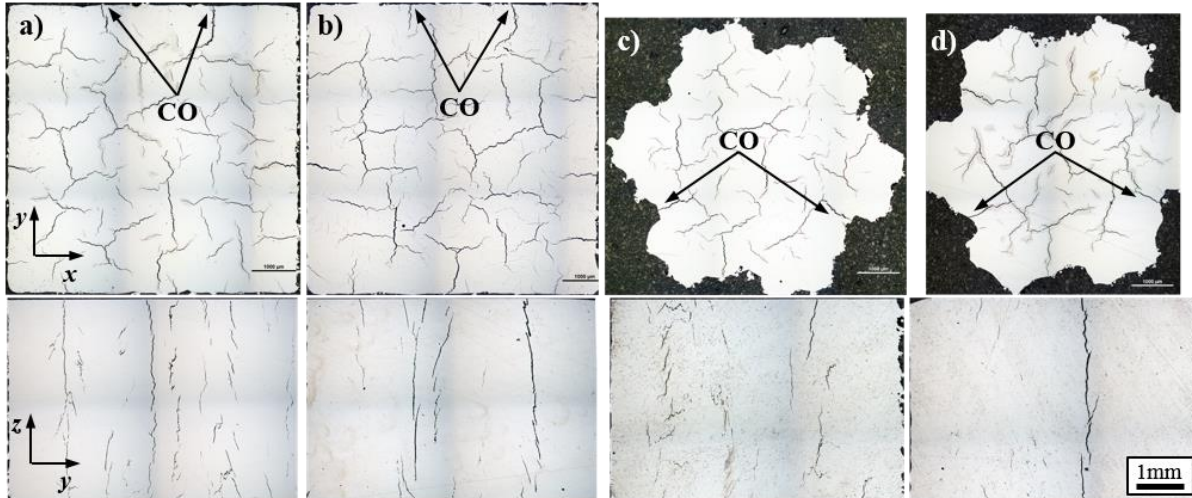
Figure 8 - (a) Hilbert [100W, 600mm.s^{-1}] and (b) Peano-Gosper [75W, 600mm.s^{-1}] scanning strategies approximately overlaid on to the deposits formed via SLM. Note that the cracking does not seem to follow the scan vectors as with the long vector length samples. Further, cracks form at an angle or perpendicular to the scan vectors, rather than directly parallel to the vectors
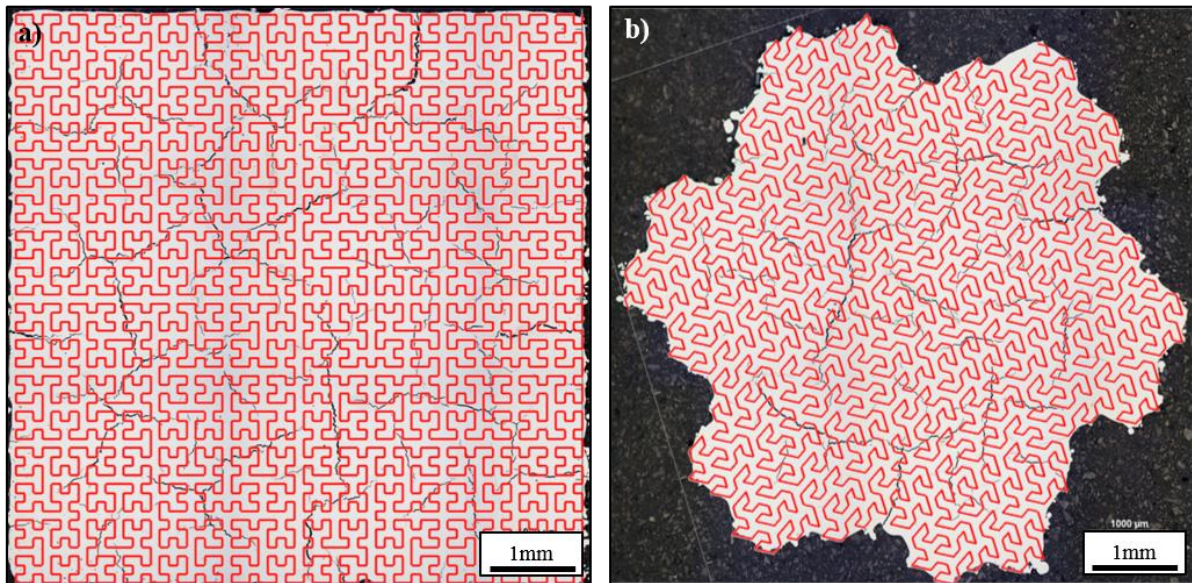
Figure 9 - Backscatter electron micrographs in the *XY* plane of the Hilbert 100W 600mm.s^{-1} sample showing: (a) bi-directional crack origin at intersection between fine and coarse equiaxed grains; (b) high angle cracking with (inset c) some sub-micron size precipitates identified along the crack surface
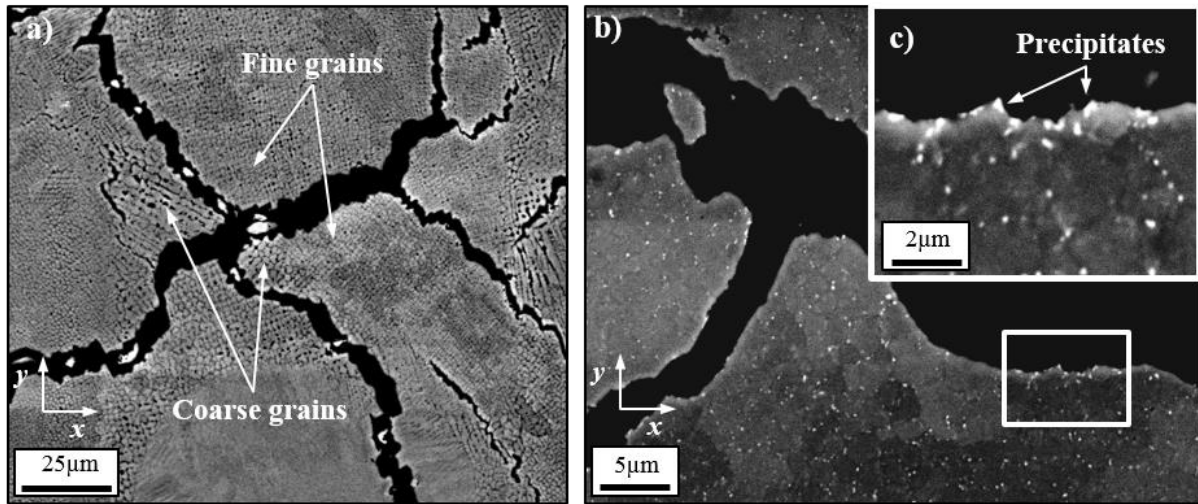
Figure 10 - EDX line scan of the 'island' scan sample showing elemental distributions across the crack surfaces. Note the lack of elemental peaks that would signify the presence of thin films at the crack boundaries.
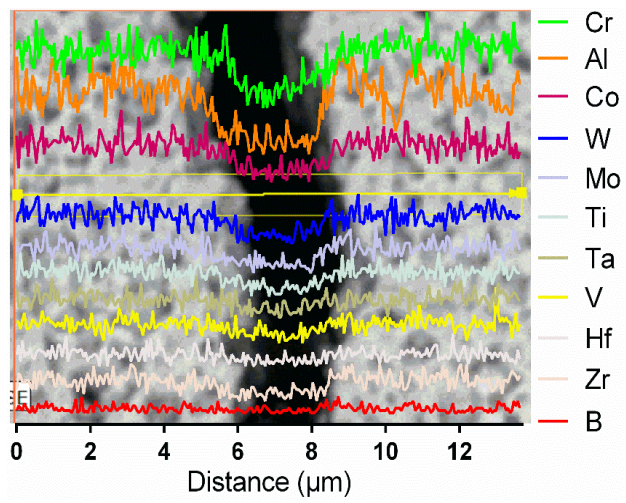
Figure 11 - Backscatter electron micrograph of the *YZ* plane of the 'island' scan sample showing: (a) the melt pool shape in red giving rise to coarse columnar grains in the core and finer, equiaxed grains at the boundary; (b) a crack following the line of intersection between a fine, equiaxed grains and coarse, columnar grains; (c) columnar dendrite surface exposed by the solidification cracking mechanism
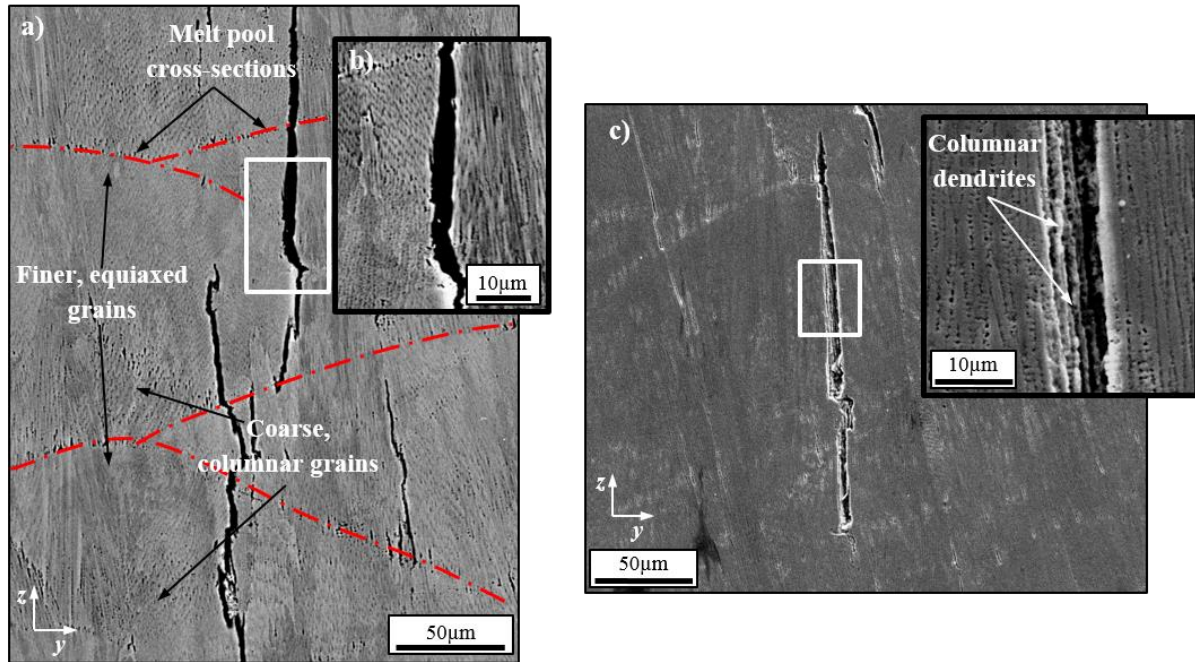
Figure 12 - Bulk density data for the samples in the XY plane (left) and YZ plane (right). The 'island' sample is represented in grey whilst the Hilbert and Peano-Gosper are in blue and red, respectively. Each pair of columns constitutes a single process parameter set identified on the x-axis label
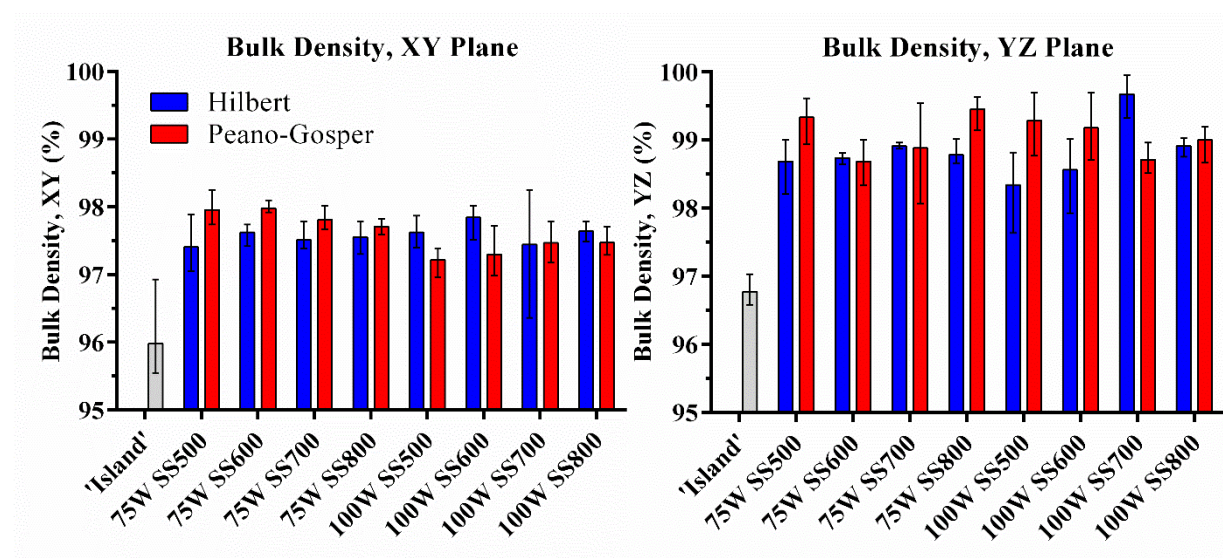
Figure 13 - Crack length density data for the 'island' (grey), Hilbert (blue) and Peano-Gosper (red) scan strategies
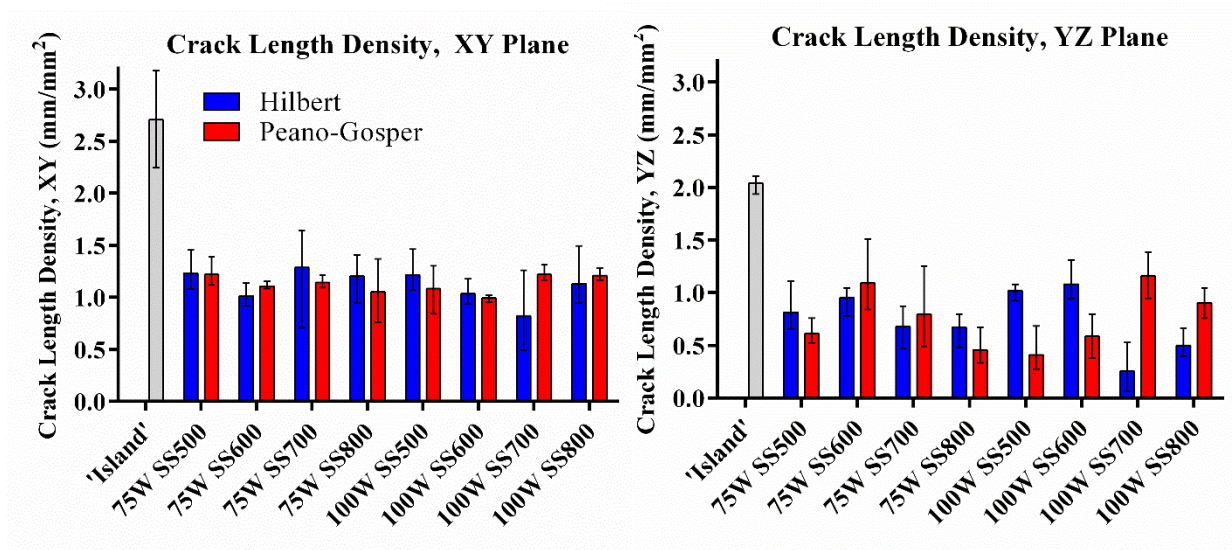
Figure 14 - Crack area density data for the 'island' (grey), Hilbert (blue) and Peano-Gosper (red) scan strategies
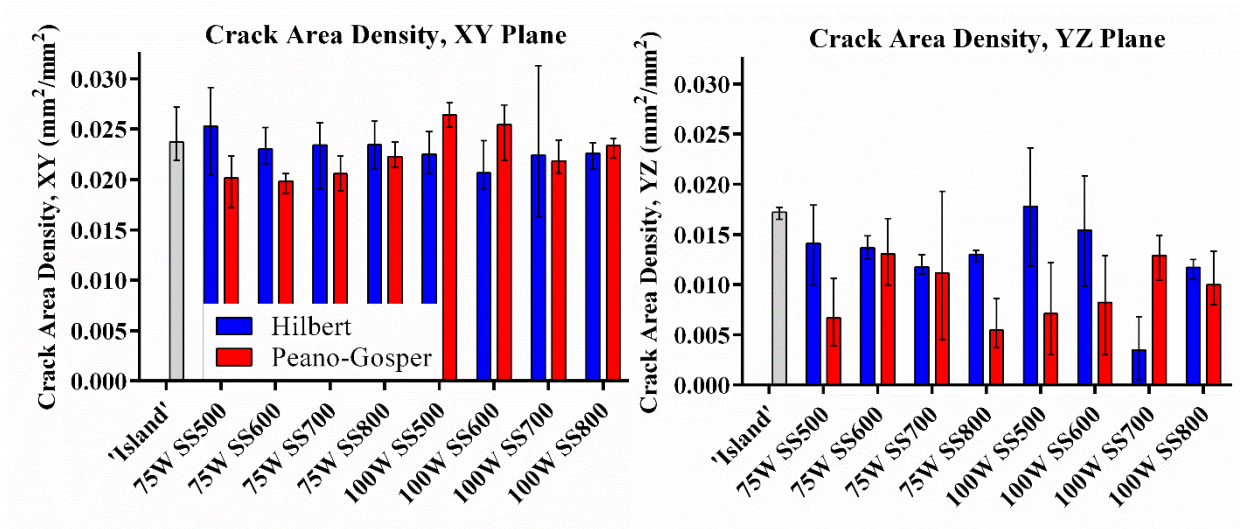
Table 1 - Elemental composition of the CM247LC powder supplied by LPW compared to the nominal composition specified for the alloy [10]

	Ni	Al	Cr	Co	Ti	Ta	Mo	W	Hf	C	B	Zr
Nominal	61.7	5.6	8.1	9.2	0.7	3.2	0.5	9.5	1.4	0.07	0.015	0.015
Actual	64.6	6.8	8.5	9.2	0.9	5.1	0.7	5.9	2.5	-	-	-

Table 2 - **Parameter combinations (laser power and laser scan speed) used to produce a total of 16 fractal scan samples (eight Hilbert and eight Peano-Gosper)**

Laser power (W)	Laser scan speed (mm.s^{-1})			
75	500	600	700	800
100	500	600	700	800